Check for updates

Volumetric live cell imaging with three-dimensional parallelized RESOLFT microscopy

Andreas Bodén[1], Francesca Pennacchietti[1], Giovanna Coceano[1], Martina Damenti [1], Michael Ratz[2] and Ilaria Testa [1]✉

Elucidating the volumetric architecture of organelles and molecules inside cells requires microscopy methods with a sufficiently high spatial resolution in all three dimensions. Current methods are limited by insufficient resolving power along the optical axis, long recording times and photobleaching when applied to live cell imaging. Here, we present a 3D, parallelized, reversible, saturable/switchable optical fluorescence transition (3D pRESOLFT) microscope capable of delivering sub-80-nm 3D resolution in whole living cells. We achieved rapid (1–2 Hz) acquisition of large fields of view (~40 × 40 µm²) by highly parallelized image acquisition with an interference pattern that creates an array of 3D-confined and equally spaced intensity minima. This allowed us to reversibly turn switchable fluorescent proteins to dark states, leading to a targeted 3D confinement of fluorescence. We visualized the 3D organization and dynamics of organelles in living cells and volumetric structural alterations of synapses during plasticity in cultured hippocampal neurons.

State-of-the-art, super-resolution methods based on targeted or stochastic switching of the fluorescence signal can reach very fine spatial information in all three spatial dimensions when combined with interferometry such as 4Pi microscopy[1–3] or other types of point spread function (PSF) engineering[4–7]. The 3D imaging ability allows access to a number of cellular structures such as the nuclear envelope, cilia and mitochondria[8].

Despite the incredible level of detail provided by such methods, volumetric imaging in living cells remains challenging, especially in regard to dynamic structures and organelles, either due to extended image acquisition times, insufficient blinking in aqueous solutions or photobleaching. Other live cell-compatible systems suffer from additional limitations. Three-dimensional structured illumination microscopy (SIM)[9,10] surpasses the diffraction limit by a factor of only two which, axially, is still around 250–300 nm. Finer spatial details can be resolved with stimulated emission depletion (STED)[11,12] and its generalization reversible saturable/switchable optical fluorescence transition (RESOLFT)[13,14] nanoscopy, where the majority of fluorescent molecules are switched to dark states in a targeted way with designed light patterns. RESOLFT nanoscopy enables two-dimensional (2D) and 3D super-resolution imaging of live cells[15,16], even in a 4Pi geometry[17], by switching reversibly switchable fluorescent proteins (RSFPs)[18,19] or dyes between metastable dark (OFF) and bright (ON) states. The reversible OFF-switching, unlike in STED, is associated with long-lived molecular states and can be efficiently accomplished with lower peak intensity illuminations and pump probe types of imaging schemes. Altogether this minimizes photobleaching from higher excited states, which is a limitation of STED, broadening the application of RESOLFT nanoscopy for time-lapse imaging. Despite the potential of achieving high spatial resolution in living cells, point-scanning implementations are relatively slow (0.5–1-ms pixel dwell time), especially for volumetric recordings (40 × 40 × 2.5 µm³, 150 megapixels, requires 20–40 h to record), limiting time-lapse imaging applications of whole-cell dynamics. Parallelized optical schemes[20] based on standing waves allow for substantial increase in recording speed and larger fields of

view in RESOLFT microscopy while maintaining its contrast and sectioning abilities[21]. With similar sinusoidal patterns, nonlinear structured illumination microscopy (NL-SIM)[22] can be applied to RSFPs as in parallelized RESOLFT[13] to achieve higher spatial resolution than linear SIM. However, this has been implemented only in total internal reflection geometry[22,23], which limits sample accessibility to the cover glass interface or in a light sheet mode where spatial resolution is nonlinearly improved in only one dimension[23].

To date, parallelized RESOLFT or NL-SIM nanoscopes have not proved capable of achieving spatial resolution <80 nm in all three spatial dimensions. To tackle this challenge, we designed an illumination pattern with highly modulated intensity along all three dimensions. The pattern exhibits an array of zero-intensity regions with sharp and nearly isotropic 3D confinement. The 'zeros', unlike in previous 3D SIM illumination[10,24], are spherically shaped making it suitable for coordinate targeted switching schemes such as STED and RESOLFT. We used the 3D modulated illumination to switch RSFPs[18] from a fluorescent (ON) to a nonfluorescent (OFF) state. The design of such parallelized optical schemes covering large fields of view of >40 × 40 µm² is crucial to speeding up recording time and increasing throughput[25]. The new 3D ability enables imaging of packed structures within living cells, such as the vimentin and actin cytoskeleton and even in the nuclear region, with 3D super-resolution. The entire mitochondrial network in a living cell, free from fixation and 3D distortion induced by immersion media, can be recorded in a few tens of seconds. The 3D resolution allows visualization of distinct compartments in small organelles such as the exosomal outer shell, mitochondrial-derived vesicles and spheroids, using light microscopy. The 3D recording can also be done over time, enabling the study of volumetric structural alterations and synaptic protein plasticity in hippocampal neurons.

Results

To achieve isotropic 3D spatial resolution, our system switches RSFPs into a metastable OFF state with a new illumination pattern (Fig. 1) created using the incoherent superposition of three

[1]Department of Applied Physics and Science for Life Laboratory, KTH Royal Institute of Technology, Stockholm, Sweden. [2]Department of Cell and Molecular Biology, Karolinska Institute, Stockholm, Sweden. ✉e-mail: ilaria.testa@scilifelab.se
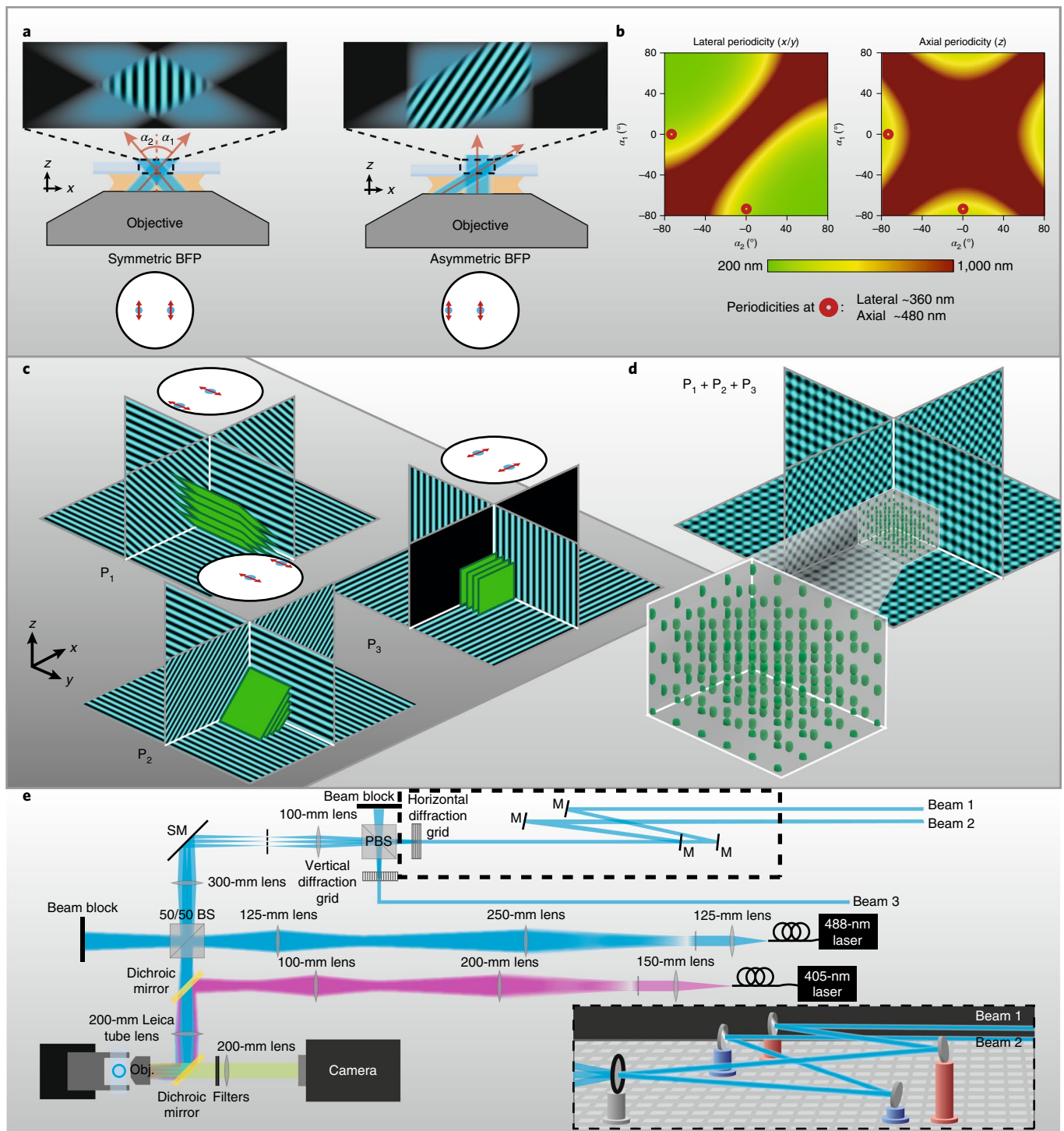
Fig. 1 | Interference based OFF-switching pattern in 3D pRESOLFT. a, 3D pRESOLFT OFF-switching pattern. Schematic illustration of coherent beam interference with different tilt. The position on the back focal plane (BFP) of the focused beams and their polarization (red double arrows) are reported below the objectives. α_1 and α_2 represent the angles between the direction of propagation of the beam and the optical z axis. **b**, 2D plots showing the lateral and axial periodicity of the resulting interference pattern as a function of α_1 and α_2. Red circles denote angles used for the tilted patterns in the implemented 3D pRESOLFT system. **c**, The three interference patterns, P_1, P_2 and P_3, are shown with corresponding beam placements on the back focal plane. Green planes illustrate the geometry of zero-intensity planes within each pattern. **d**, The incoherent superposition of P_1, P_2 and P_3 results in 3D confined volumes, emphasized here by green volumes. **e**, Schematic illustration of the optical setup used to create the OFF-switching and multifocal patterns. Obj., objective; M, dielectric mirror; SM, silver mirror. Inset at bottom right shows a 3D view of the mirror and grid configuration used to hit the grids at an angle, resulting in the tilted patterns P_1 and P_2 (Supplementary Fig. 3).

different standing wave patterns. Each standing wave pattern is generated by the interference of two coherent plane waves, exiting the objective at predefined directions. Two of the standing wave patterns, P_1 and P_2, are tilted with respect to the optical axis. This tilt gives the final pattern its axial modulation and is achieved by shifting the two focused spots on the back focal plane so that
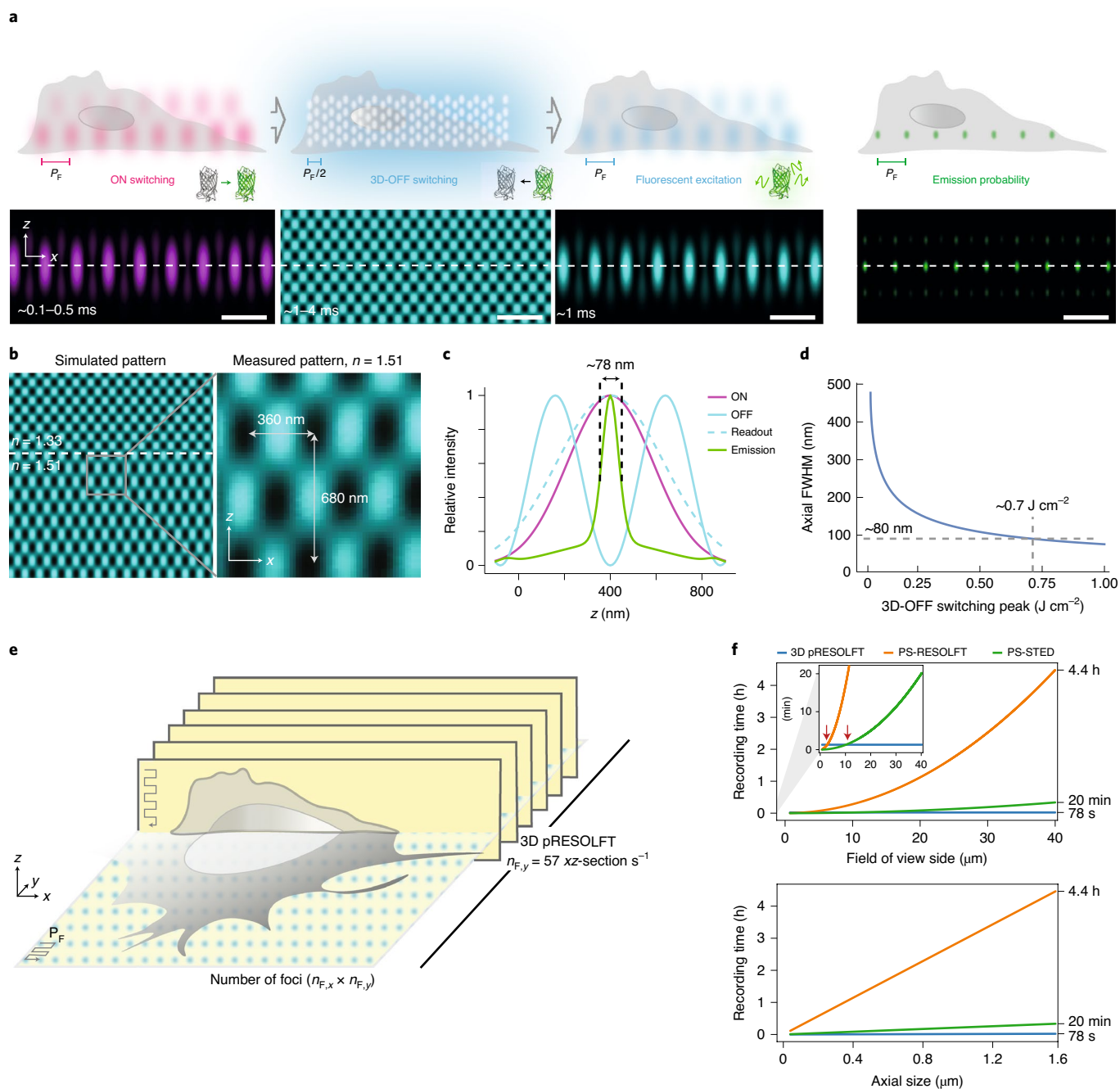
Fig. 2 | 3D pRESOLFT imaging scheme and parallelization. a, Top: 3D pRESOLFT acquisition schemes and recording time. Bottom: illumination scheme applied sequentially in 3D pRESOLFT imaging and related simulation of light patterns. P_F, periodicity of the microlenses-foci in the sample plane. Scale bars, 1mm. **b**, Left: simulation of the OFF-pattern along a lateral and the optical $x–z$axis. Axial compression of the pattern due to the refractive index interface between the cover glass and sample is illustrated. Right: experimentally measured OFF-pattern. **c**, Axial profile of illumination patterns (ON, OFF and readout) with the resulting expected emission distribution at ~78nm FWHM from Gaussian fit. **d**, Dependence of fluorescence confinement on illumination energy calculated as the peak energy of each OFF-pattern P_1 and P_2. **e**, Illustration of the recording modalities of 3D pRESOLFT, where the sample can be imaged both scanning the whole volume for isotropic resolution (xyz mode, P_1–P_3 OFF-pattern) or axially slicing the sample simultaneously at each focal position for temporal resolution (xz or yz mode with P_1–P_2 OFF-pattern). **f**, Comparison of recording times needed for volumetric recording in a point-scanning (ps) approach with 400µs (RESOLFT, orange line), 30µs (STED, green line) and a parallelized approach with 6-ms dwell time (3D pRESOLFT, blue line). The recording times are calculated for a scanning step of 50nm and either axial size fixed at 1.6µm while increasing lateral field of view (top) or for a constant 40×40-µm^2 area while increasing axial size (bottom). Inset shows the graph with a rescaled y-axis to visualize the crossings near the origin.

they are asymmetrically positioned with respect to the optical axis (Fig. 1a). The third pattern, P_3, which is symmetric on the back focal plane, confines the volumes in the final, lateral, dimension. The

exact axial and lateral periodicities of the pattern can be tuned by changing the position of the focused beams on the back focal plane. Since the periodicity of the pattern in a given direction is inversely

proportional to the fluorescence confinement at a certain intensity, tuning the periodicities will affect the properties of the imaging system. For the imaging demonstrated here, we chose the axial and lateral periodicities of 480 and 360 nm, respectively, that minimized axial periodicity and thus maximized potential axial resolution (Supplementary Fig. 1). Each standing wave pattern creates planes of zero intensity in the illuminated volume, as shown in Fig. 1c. The points where planes from all three patterns intersect will be the centers of the resulting zero-intensity volumes (Fig. 1d), which are generated in the whole 3D volume, resembling a honeycomb. This new 3D pattern is mathematically described in Supplementary Note 1 and realized in practice according to the optical scheme illustrated in Fig. 1e and Supplementary Fig. 3 (Supplementary Note 2).

When combined with RSFPs such as rsEGFP2 (ref. [18]) or Dronpa(M159T)[26], the blue light first induces fluorescence excitation and then OFF-switching while the visible ultraviolet light switches the molecules back into the ON-state. This transition is reversible and can endure >1,000 cycles before irreversible photodamage[18].

Starting with all RSFPs at equilibrium in the ON-state, OFF-switching will imprint patterns of state distribution into the sample which then, under fluorescent excitation, translates into a spatial pattern of expected emission. In our current implementation (Fig. 2a), a multifocal pattern at 405 nm is used to imprint an initial state distribution during ON-switching. The OFF-switching pattern is used to confine into the OFF state the majority of RSFPs located at the periphery of the foci in all spatial directions. The remaining RSFPs in the ON-state create a pattern consisting of distinctly separated and sharply 3D-confined subdiffracted volumes. As these volumes are probed with another multifocal pattern of blue light at 488 nm, we image the relative fluorophore density in each 3D-confined volume of the focal plane onto the camera.

We measured the effective OFF-switching pattern by scanning fluorescent beads across the pattern (Fig. 2b) to check the periodicity (680 nm in Mowiol) and the quality of the destructive interference in the zero (<3%). If, on the other hand, a sample mounted in water is used, the mismatch of refractive indices between the glass and sample (1.51 and 1.33, respectively) results in compression of the pattern from 680 nm in glass/Mowiol to 480 nm in the sample, which gives nearly isotropic confinement. The three patterns (ON, OFF and readout) must be spatially aligned with matching periodicities (Fig. 2c); the alignment procedure is described in Supplementary Note 2. Given the rsEGFP2 switching kinetics (Supplementary Note 3) and a peak energy of 0.7 J cm^{-2} for $P_1 + P_2$, the resulting confined fluorescent volume will have a full width at half maximum (FWHM) of around 78 nm (Fig. 2c,d) along the optical axis and 59 nm along the lateral x direction. The addition of P_3 with a peak intensity of 0.7 J cm^{-2} confines the volumes also along the lateral y axis to a FWHM of 59 nm. The dependence between axial FWHM and energy of OFF-switching illumination is shown in Fig. 2d. The size of the confined volumes reflects the potential

resolution of the imaging system for a realistic number of fluorophores and measured RSFP kinetics (Supplementary Notes 3 and 7).

Although resolution extension beyond the diffraction limit stems from the OFF-switching pattern described above, the final image quality is highly dependent on multifocal patterns[21]. This minimizes the amount of out-of-focus emission that deteriorates the image signal-to-noise, and also gives the flexibility of ON-switching and reading out only a subset of zero volumes, which reduces the crosstalk and enhances the signal-to-noise[21]. 3D pRESOLFT images are acquired by scanning the sample across the patterns for a number of scanning steps largely reduced compared to a single-beam, point-scanning imaging scheme, shortening the recording time of a volume ($40 \times 40 \times 1.6\,\mu m^3$) from 4.4 h to 78 s (Fig. 2e,f). The duration of each scanning step is that of a complete RSFPs cycle, resulting in a dwell time of 1–6 ms. Considering a dwell time of 30 μs as in 3D STED, and 6 ms for 3D pRESOLFT, the acquisition time is still substantially reduced by the parallelization, from 20 min to 78 s, enabling new dynamic studies previously inaccessible. We can operate 3D pRESOLFT in two modalities: the xz mode features axial and x-lateral spatial super-resolution (<80 nm) while y-lateral diffraction is limited (~180 nm) by the use of P_1–P_2 for OFF-switching. In this mode we can acquire a volumetric measurement per second and up to 10–20 volumes. In contrast, the xyz mode uses the OFF-switching pattern provided by P_1–P_2–P_3 for nearly isotropic spatial resolution improvement. Here the scanning steps increase since the y direction also needs to be sampled. Typically, recording of the entire volume can vary from 30 to 80 s and we can record up to three volumes; the number of volumes recorded depends on the number of cycles that can be borne by the RSFPs before irreversible photobleaching. All imaging parameters are reported in Supplementary Table 5.

To avoid not having to rely solely on theoretical resolution claims, we focus on practical demonstrations of achievable resolution. To this end we imaged several fluorescently labeled beads across the whole field of view with the full 3D confinement (P_1–P_2–P_3) and provide line profiles and Fourier ring correlation (Supplementary Fig. 11). Quantifications are performed on both raw and deconvolved data. Deconvolution of 3D pRESOLFT images (Supplementary Note 5 and Supplementary Fig. 8) is not mandatory for resolving fine structures but it can help in suppressing the background originating from residual RSFPs in the ON-state. The PSF used for deconvolution is based on measured data of RSFP kinetics (Supplementary Tables 1–4).

We provide theoretical calculations and computational simulations to address the potential resolution of the system for a given number of rsEGFP2 organized in two sheet-like structures at different axial distances and experimentally tested illumination energies (Fig. 3a and Supplementary Notes 6–8). This theoretical framework will help predict the imaging performance for different applications where proteins of varying abundance and spatial organization need to be imaged. The results of the simulation

Fig. 3 | Resolution assessment in 3D pRESOLFT. a,b, Simulated (**a**) and measured (**b**) 3D pRESOLFT imaging. The virtual sample is created as two labeled sheets with varying axial separation to mimic the real sample. The sheets are labeled with 20 fluorophores per $20 \times 20 \times 20$-nm³ voxel. The data are simulated and acquired in xz mode. Images have been smoothed with a 20-nm Gaussian filter to aid visualization. The line profiles are fitted with the expected PSF (Supplementary Notes 3 and 4). The widths and separation between peaks are reported, and line profiles are measured in raw images. The experimental data are representative from a set of $n = 6$ similar volumes. Scale bars, 1 mm (**a,b**). **c**, Volumetric recording of vimentin-rsEGFP2 imaged in xz mode. Two zooms from the same single 3D stack comprising $n = 60$ slices, simultaneously recorded, are shown paired with the corresponding enhanced (enh.) confocal image recorded with no OFF-switching. New features of the vimentin cytoskeleton are axially resolved at cell–cell contacts. Scale bars, 1 μm. Norm. fluo., normalized fluorescence intensity. **d**, Representative volumetric imaging of exosomes labeled with CD63-rsEGFP2 and isotropic 3D resolution, and shown as an axially color-coded projection. The volume is taken from a set of $n = 3$ similar volumetric recordings. The outer membrane localization of CD63 is visible only in the 3D pRESOLFT images, as shown in four examples of single vesicles across the $43 \times 43 \times 1.1$-μm³ volume (right). Confocal and super-resolved images (represented by the asterisk) are deconvolved (20 iterations) as described in Methods. All line profiles are drawn across the arrow in the 3D pRESOLFT (data denoted by black dots, fitted model by black line) and confocal images (gray line). Cells are U2OS. Scale bar, 5 μm (insets, 200 nm).

show that 3D pRESOLFT can differentiate axial structures sized <80 nm (FWHM of Gaussian fit) at a distance approaching 100 nm (Fig. 3a). Real imaging data of similar structures (Fig. 3b) consisting of actin fibers confirm the simulation, showing filaments widths down to 70–80 nm and a peak-to-peak separation of 116 nm.

As a complementary note, it should be recognized that there is no theoretical band limit to the imaging system—the volumes are confined in all directions to a size determined by the power and duration of the OFF-switching illumination. Very sharp confinement will, however, alter the signal-to-noise and signal-to-background
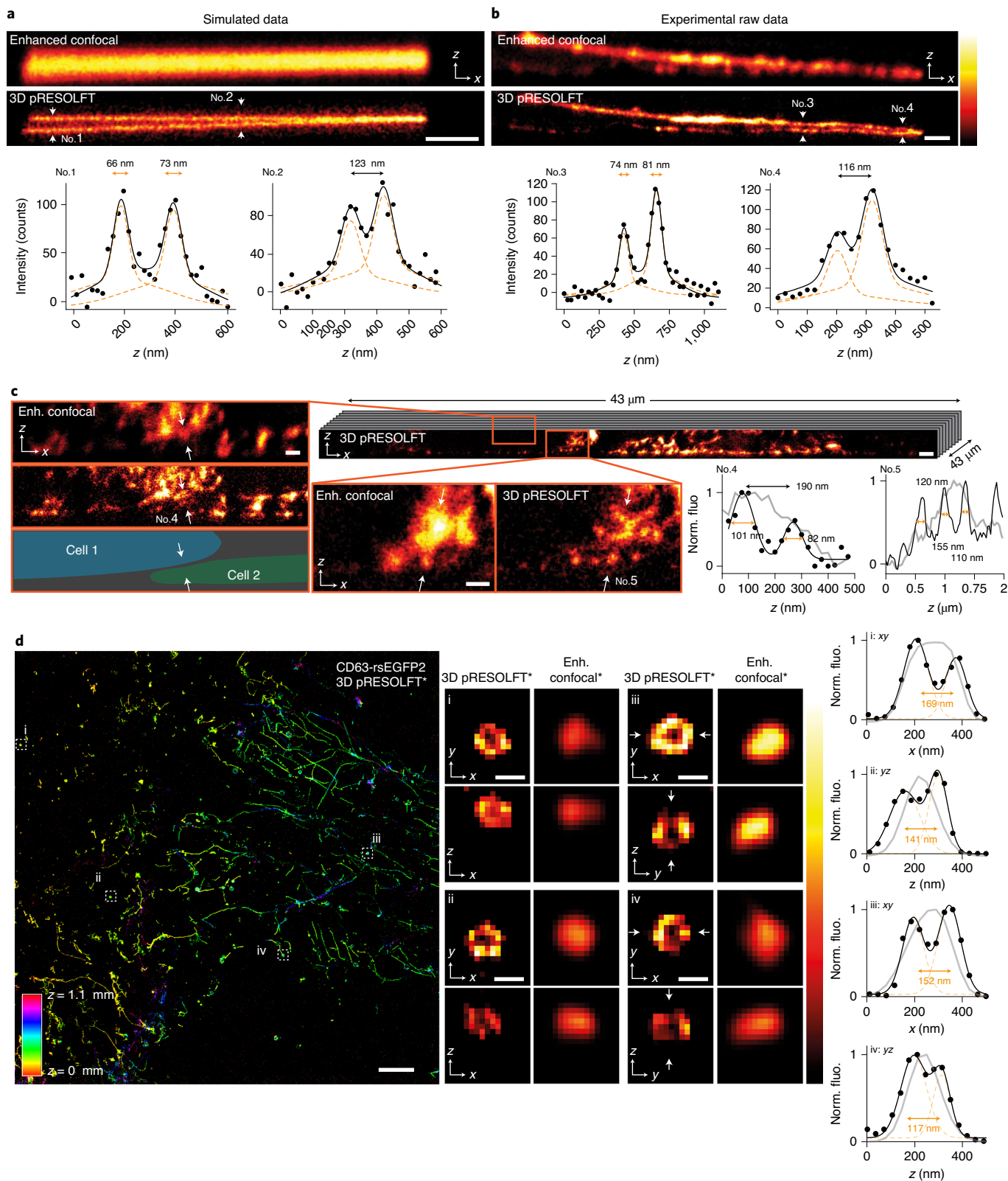
levels in ways that are dependent on the fluorophore and labeling characteristics in a nontrivial way[27]. Other parameters, including labeling density and type of structure being imaged, also alter the effective resolution of the system (Supplementary Fig. 10).

We demonstrate the use of 3D pRESOLFT for biological imaging by visualizing widely differing types of structure, both filamentous and vesicular, with fine 3D precision (Fig. 3b,c). Endogenously labeled intermediate filament structures stably expressing vimentin-rsEGFP2 in U2OS cells are well resolved, even in axially extended cellular zones such as perinuclear regions typically highly packed or at cell-to-cell contact sites (Fig. 3c). The raw imaging data clearly show the fine border between two adjacent cells, as well as distinct bundles (Fig. 3c, insets), which are not visible in the enhanced[21] (~350-nm axial resolution) confocal image acquired without 3D OFF-switching. Thus, 3D pRESOLFT allows observation and study of the entire intermediate filaments network, paving the way for future imaging studies in multicellular systems. We also imaged exosomes (Fig. 3d), dynamic organelles that are of growing importance in medical research due to their role as mediators of intercellular communication in various physiological and pathological processes[28]. The diameter of exosomes can range from 50 to 170 nm and, despite their importance, many fundamental aspects including origin, biogenesis and fate remain difficult to study due to their small size. The 3D pRESOLFT images recorded in isotropic mode unraveled localization of the marker protein CD63 in the outer membrane of exosomes, which was not resolved in the conventional image. These recordings provide a demonstration of exosomal structural features in living cells using light microscopy.

Other dynamic and light-sensitive organelles—such as mitochondria with the outer membrane marked with rsEGFP2—can be investigated with the spati-temporal resolution of 3D pRESOLFT (Fig. 4). The dynamics of mitochondria are visualized within seconds by time-lapse imaging of a cell from the side view (Fig. 4a and Supplementary Video 1), where the 3D reorganization and morphological changes of the outer membrane are disentangled by the high axial resolution of the method. Volumetric recordings across the large cellular volume are not possible with point-scanning 3D super-resolution systems, because the organelles are too dynamic (Supplementary Fig. 11). On the other hand, our system enables capture of dynamics without sacrificing spatial precision and allows one to distinguish axially the upper and lower membrane compartments (Fig. 4b).

To further explore the 3D isotropic potential of our method, we recorded the whole 3D mitochondrial network in *xyz* mode (Fig. 4c), which represents the volumetric data of a whole living cell using light microscopy at a resolution <80 nm (Supplementary Video 2). The zoomed-in views highlight the ability of the system to accurately measure distinct organelles as well as small mitochondria-derived vesicles (MDVs) budding out of the outer membrane. After volumetric recording, the mitochondria network maintains a tubular morphology and an active membrane potential supporting the live cell compatibility of the method (Supplementary Note 9 and Supplementary Fig. 13). In a similar way, we acquired the full volume of the actin cytoskeleton at different time points (Fig. 4d and Supplementary Video 3). Intertwined actin fibers can

be disentangled by the spatial accuracy of 3D pRESOLFT and followed over time, showing twisting and sliding. The new imaging ability to resolve the 3D extension of small structures and to correlate their protein relocalization upon stimulation could foster a series of new functional and structural studies. Accordingly, we used the system to investigate the dynamic structural alterations in mitochondria induced by oxidative damage, as often observed in models of aging and the progression of diseases[29]. We used two distinct drugs, antimycin A and carbonyl cyanide m-chlorophenylhydrazone (CCCP), which selectively affect mitochondrial respiration. We observed volumetrically the whole mitochondrial network in the same cells before and after treatment (Fig. 5a). The outer membrane topology completely changed upon treatment, from tubular to a series of different structures including fragments, small vesicles and spheroids that previously could be visualized only using electron microscopy[30,31] (Fig. 5b). Mitochondrial fragments, associated with mitophagy, are hardly distinguishable from spheroids with imaging methods lacking 3D super-resolution, since spheroids typically contain an inner lumen or various indentations composed by outer membrane segments visible only in 3D pRESOLFT images (Fig. 5b and Supplementary Fig. 14). We quantified the volume of fragments and spheroids as the ratio of outer and inner volumes, and measured its structural dynamics (Fig. 5c). In 2D image projections spheroids are also often confused with ring-shaped mitochondria even if they are functionally very different, because they are associated with compromised and healthy mitochondria, respectively. While mitochondrial fission and budding out of vesicles are observed under control conditions, as well as in the few minutes following drug treatment, the formation of spheroids and an increased number of small vesicles was visualized only following treatment (Fig. 5d,e).

Subsynaptic structures, such as curvilinear actin bundles, postsynaptic densities and other scaffold proteins, undergo restructuring during synaptic activity to control receptor numbers and correct downstream signaling[32]. High-resolution imaging methods are needed to resolve the fine distribution of such proteins in the architecture of small and packed dendritic spines[33,34]. In this study, we focus on 3D imaging of actin and homer (Fig. 6 and Supplementary Video 4) in dendrites of mature hippocampal neurons under basal activity and chemically induced long-term potentiation (LTP). The volumes were acquired in full 3D isotropic mode. While the projection image (Fig. 6a, regions of interest (ROI) 1–3) shows fine actin structures and the topology of dendrites, it is hard to interpret the real shape of these protrusions, which can readily be categorized as filopodia or large accumulations. We then provided a 3D rendering of several regions (Fig. 6a, right) which allowed the untwining of packed regions and observation of a variety of spine morphologies appearing as hammer-, cup- or spherical-shaped elongating in all three spatial directions. The same structures were further investigated several minutes after LTP stimulation, showing the formation of new actin structures to accommodate an enlargement of the spine head (Fig. 6a, ROI 4). We performed the same treatment on homer, whose restructuring during plasticity is poorly understood[32,35]. We observed the 3D organization of >300 homer nanodomains on a single volumetric recording, highlighting the need for 3D imaging in a comprehensive investigation of the homer

Fig. 4 | Four-dimensional imaging and rendering in full-length human cells. a, The time series consists of 3D pRESOLFT* (50 iterations) volumes recorded over 2 min at high temporal resolution (1.6 s per volume) in *xz* mode, capturing axial mitochondrial dynamics. Each reported *xz* image is selected from a volume consisting of 21 slices (Supplementary Video 1). Scale bar, 1 μm. **b**, Zoomed-in view of single mitochondria showing the ability of 3D pRESOLFT to disentangle the upper and lower outer mitochondrial membranes, even axially at a distance of ~110 nm. The images are deconvolved. Scale bars, 500 nm. **c**, Volumetric rendering containing the whole mitochondrial network recorded in isotropic *xyz* mode. Zoomed-in views show a tubular mitochondrion above a vesicular structure segmented in red and green, respectively. The volumetric views show raw reconstructed data, while the *xz* slice (bottom right) is deconvolved (40 iterations) (Supplementary Video 2). The mitochondrial dynamics reported are representative of *n* = 7 similar time-lapse recordings. Scale bar, 2 μm (insets: left, 500 nm; right, 200 nm). **d**, Two sequential volumetric recordings of the actin cytoskeleton in *xyz* mode. Dynamics structures are shown in blue. Zoomed-in views below highlight a dynamic helical structure formed by twisting of intertwined filaments. Cells are U2OS. Scale bars, 1 μm (left) and 500 nm (right).

population on several dendrites (Fig. 6b). The quantification of homer density was performed along the three spatial directions allowing the determination of volumes, which enables observation of the differences between homer's disks and spheres previously hidden in 2D projections. This is especially important when quantifying homer morphological changes during plasticity. Here, homer

densities that would appear similar in size in lateral images acquired before and after LTP treatment show instead a clear axial elongation and 3D redistribution (Fig. 6c). With this new precision, we quantified tens of homer nanovolumes before and after LTP and observed that some underwent a substantial increase while other subgroups decreased or remained unaltered (Supplementary Fig. 15).
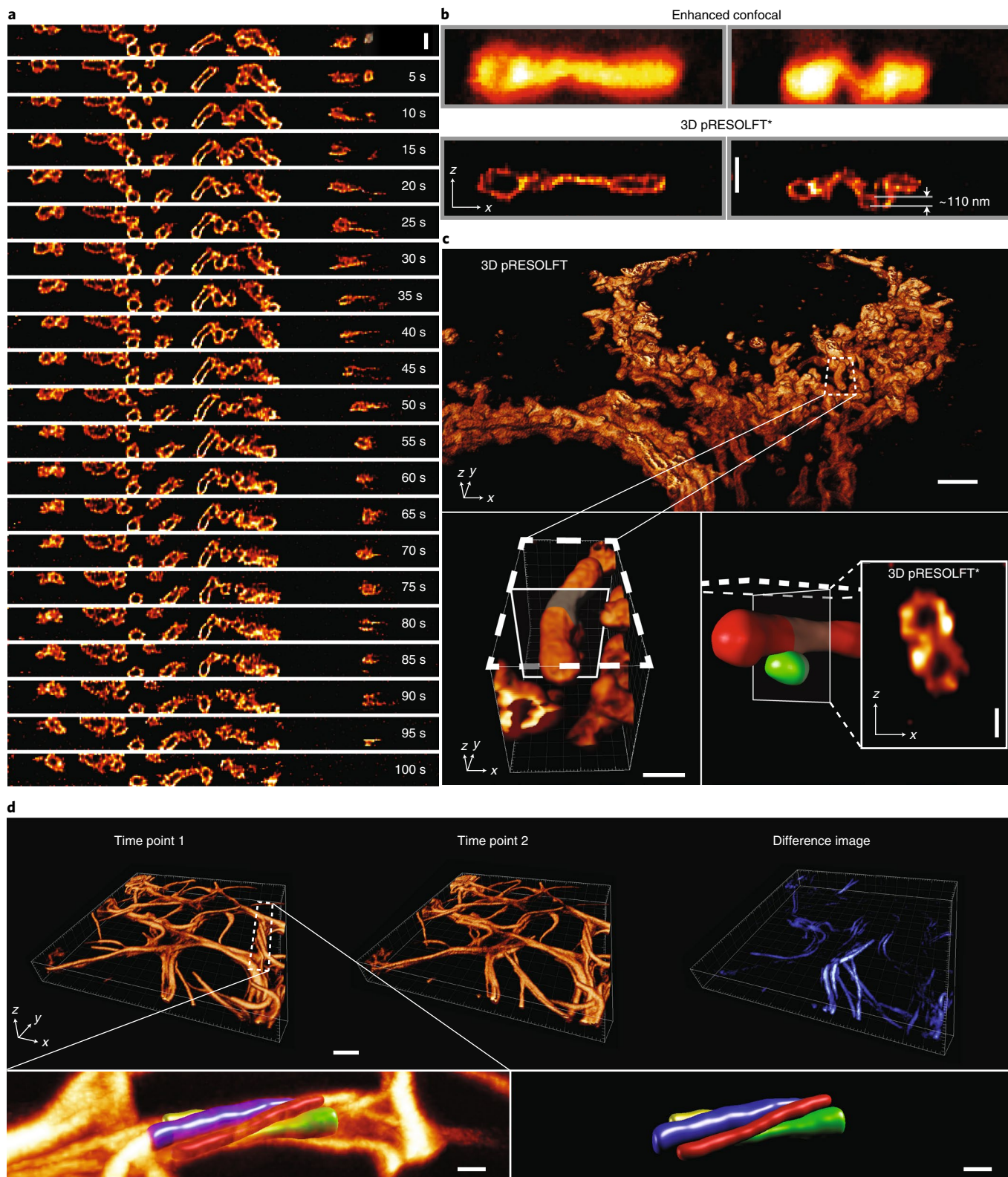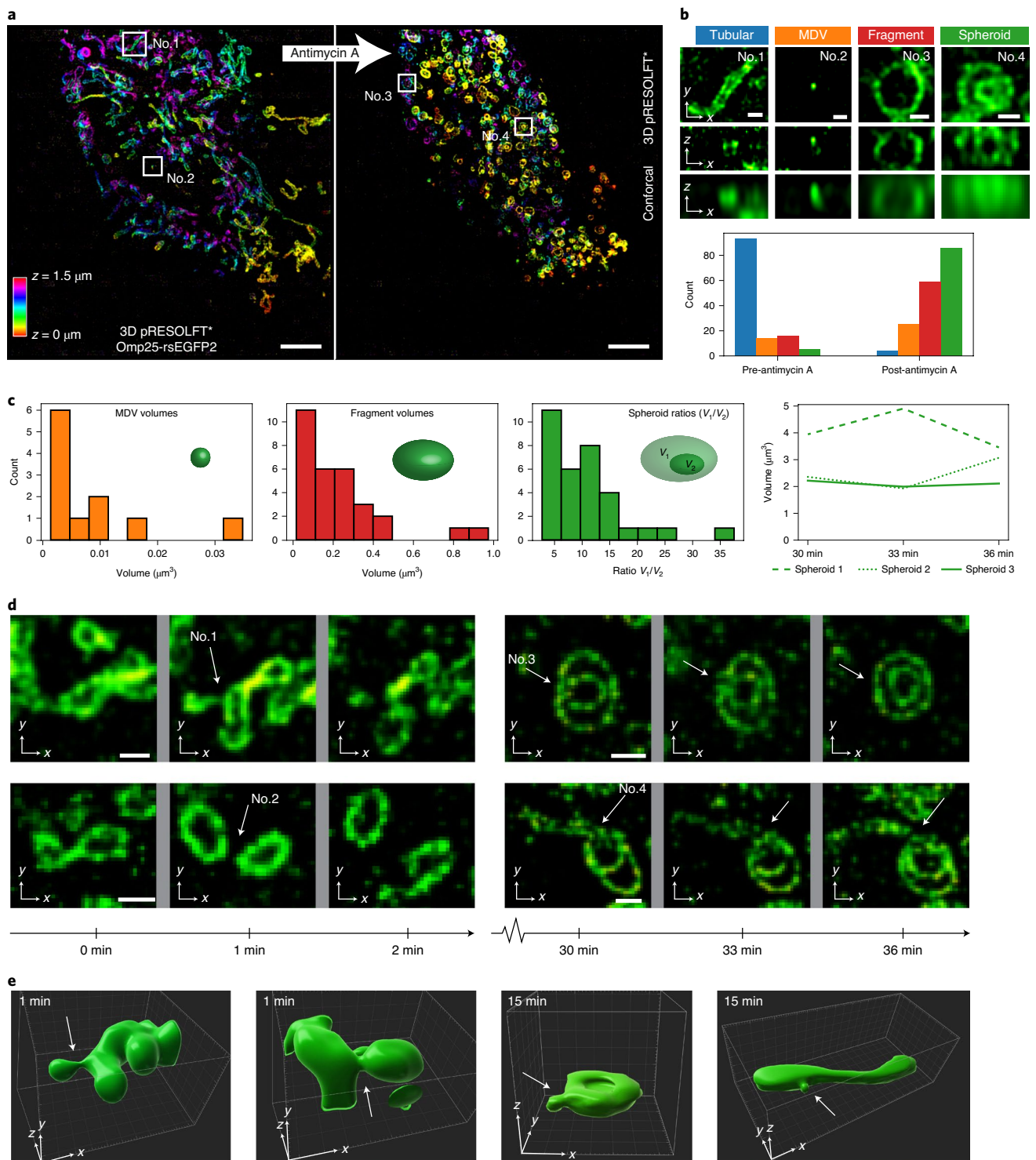
Fig. 5 | Structural alteration of mitochondria following oxidative stress. a, Volumetric imaging of the whole mitochondrial network recorded with 3D pRESOLFT* (ten iterations) in isotropic *xyz* mode to resolve outer membrane topology in 3D. The same cells were observed before and after treatment with antimycin A. Images are color coded for axial depth. Scale bars, 5 μm. **b**, Zoomed-in views showing the fine 3D morphology of mitochondria in healthy and compromised organelles as tubular complexes, MDVs, fragments and spheroids. This morphological variety is visible only in the super-resolved images—blurring with a 3D Gaussian kernel 230 × 230 × 500 nm³ making fragments and spheroids undistinguishable. Histogram quantifying the whole tubular network restructured into different vesicular organelles after oxidative stress in *n* = 3 cells. Scale bars, 500 nm. **c**, Histograms showing the volume distribution of MDVs, fragments and spheroids quantified as the ratio of outer shell-to-lumen volume. V_1, volume of the outer spheroid shell; V_2, volume of the inner spheroid's core. The right-hand graph shows the temporal structuring of spheroids in CCCP-treated cells captured 30–36 min after treatment. **d**, *xy* slices from 3D pRESOLFT* (30 iterations) volumetric time-lapse taken at 0–2 min (left) and 30–36 min (right) after CCCP treatment. White arrows indicate mitochondrial outer membrane vesicular protrusions and fission (nos. 1 and 2), spheroid formation from tubular mitochondria, fusion at the tips (no. 3) and fusion in the middle followed by spheroid fission (no. 4). Images were taken from a set of *n* = 6 cells imaged at different time points after CCCP treatment. Scale bars, 500 nm. **e**, 3D renderings of mitochondrial structural alteration highlighting outer membrane protrusion during fission and the formation of MDVs budding out from tubular mitochondria and spheroids (arrows, 500 nm).
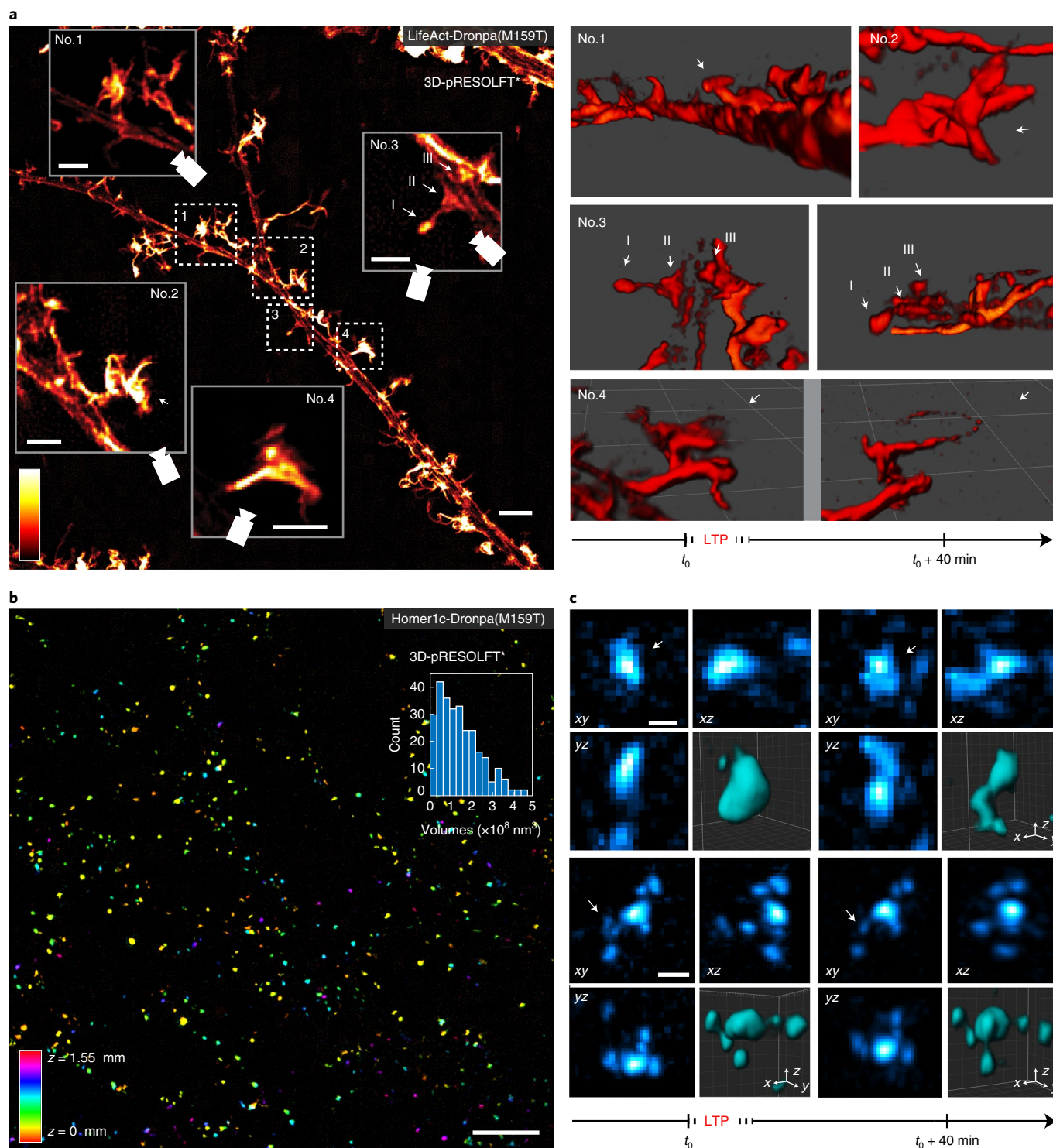
Fig. 6 | Intrasynaptic neuronal imaging with isotropic 3D pRESOLFT. a, Fine actin structures in dendritic spines of mature hippocampal neurons recorded with 3D pRESOLFT* (20 iterations) are shown at a maximal intensity projection of 1.5-μm axial depth. The renderings of four areas (right) viewed, according to the camera symbols, unravel the full 3D extension of the structures facilitating the recognition of hammer- and cup-shaped spine heads. ROI 4 highlights the formation of fine structures 40 min after LTP stimulation in four dimensions (Supplementary Video 4). In this experiment, one volumetric area was imaged before LTP stimulation and the same volume was imaged following LTP stimulation along with $n = 11$ additional volumes. Scale bar, 5 μm (insets, 1 μm). I, II and III represent actin bundles inside the spine head, at the anchor point with the dendritic shaft and protruding along the optical axis. The arrows indicate either actin budles protruding in 3D (close to I, II, III) or actin substructures growing in a dendritic spine head upon LTP treatment. t_0 is the time where the neuron was in normal buffer before chemical LTP stimulation. **b**, Volumetric distribution of Homer1c labeled with Dronpa(M159T) and imaged with 3D pRESOLFT. The inset shows quantification of the area for the 321 homer densities acquired simultaneously. Scale bars, 5 μm. **c**, Illustrative ROI, presented as maximum intensity projection and 3D rendering, showing dynamic restructuring following LTP of density into axially elongated disks hardly visible in *xy* views. Scale bars, 250 nm (top), 500 nm (bottom).

These distinct dynamic responses point to synaptic heterogeneity, which can now be finely dissected given the increased throughput, 3D precision and live cell compatibility of our method.

Discussion

We present 3D pRESOLFT, a new approach to 3D super-resolution imaging compatible with live cell recording and operation in large fields of view. The new imaging abilities of 3D pRESOLFT enable, in living cells, 3D time-lapse imaging with high levels of spatial detail. Previously, recordings of organelle dynamics in whole cells were feasible only in fixed cells given the enormous trade-off in spatiotemporal resolution. In contrast, 3D pRESOLFT increases the recording speed, which will permit the design of single-cell studies at nanoscale spatial resolution.

The fluorescent emission of RSFPs can be finely confined in 3D using a novel combination of interference patterns. Our technique relies on the use of reversibly switchable fluorophores and is demonstrated here using rsEGFP2 and Dronpa (M159T), but the concept translates to other green- and red-emitting, reversibly switching probes[19]. The resulting images show both lateral and axial resolution <80 nm without previous information or processing. A post-acquisition deconvolution with a PSF carrying RSFP photoswitching insights can be applied to enhance contrast, but is not a mandatory requirement for the method in overcoming the diffraction limit. The same interference pattern can be used in other imaging techniques, such as 3D structured illumination microscopy and its nonlinear version, which allows for novel multiplex and versatile imaging platforms.

Although robust proof-of-concept demonstrations are provided herein, further developments in labeling strategies, such as transient binding[36], will have a major impact in extending the duration of volumetric time-lapse imaging. For future imaging studies in deep tissues and other scattering samples, the implementation of adaptive wavefront corrections[37] may prove essential for the preservation of light patterns within these complex media. We believe that this technique and its future multicolor developments will be of great use for numerous studies in cellular biology aiming to analyze the 3D distribution and dynamics of organelles and molecules in living, intact biological systems.

Online content

Any methods, additional references, Nature Research reporting summaries, source data, extended data, supplementary information, acknowledgements, peer review information; details of author contributions and competing interests; and statements of data and code availability are available at https://doi.org/10.1038/s41587-020-00779-2.

References

1. Schmidt, R. et al. Spherical nanosized focal spot unravels the interior of cells. *Nat. Methods* **5**, 539–544 (2008).
2. Shtengel, G. et al. Interferometric fluorescent super-resolution microscopy resolves 3D cellular ultrastructure. *Proc. Natl Acad. Sci. USA* **106**, 3125–3130 (2009).
3. Aquino, D. et al. Two-color nanoscopy of three-dimensional volumes by 4Pi detection of stochastically switched fluorophores. *Nat. Methods* **8**, 353–359 (2011).
4. Huang, B., Wang, W., Bates, M. & Zhuang, X. Three-dimensional super-resolution imaging by stochastic optical reconstruction microscopy. *Science* **319**, 810–813 (2008).
5. Juette, M. F. et al. Three-dimensional sub-100 nm resolution fluorescence microscopy of thick samples. *Nat. Methods* **5**, 527–529 (2008).
6. Pavani, S. R. et al. Three-dimensional, single-molecule fluorescence imaging beyond the diffraction limit by using a double-helix point spread function. *Proc. Natl Acad. Sci. USA* **106**, 2995–2999 (2009).
7. Willig, K. I., Harke, B., Medda, R. & Hell, S. W. STED microscopy with continuous wave beams. *Nat. Methods* **4**, 915–918 (2007).
8. Huang, F. et al. Ultra-high resolution 3D imaging of whole cells. *Cell* **166**, 1028–1040 (2016).
9. Gustafsson, M. G. L. et al. Three-dimensional resolution doubling in wide-field fluorescence microscopy by structured illumination. *Biophys. J.* **94**, 4957–4970 (2008).
10. Shao, L., Kner, P., Rego, E. H. & Gustafsson, M. G. Super-resolution 3D microscopy of live whole cells using structured illumination. *Nat. Methods* **8**, 1044–1046 (2011).
11. Hell, S. W. & Wichmann, J. Breaking the diffraction resolution limit by stimulated emission: stimulated-emission-depletion fluorescence microscopy. *Opt. Lett.* **19**, 780–782 (1994).
12. Klar, T. A., Engel, E. & Hell, S. W. Breaking Abbe's diffraction resolution limit in fluorescence microscopy with stimulated emission depletion beams of various shapes. *Phys. Rev. E* **64**, 066613 (2001).
13. Hell, S. W., Jakobs, S. & Kastrup, L. Imaging and writing at the nanoscale with focused visible light through saturable optical transitions. *Appl. Phys. A Mater. Sci. Process.* **77**, 859–860 (2003).
14. Hofmann, M., Eggeling, C., Jakobs, S. & Hell, S. W. Breaking the diffraction barrier in fluorescence microscopy at low light intensities by using reversibly photoswitchable proteins. *Proc. Natl Acad. Sci. USA* **102**, 17565–17569 (2005).
15. Grotjohann, T. et al. Diffraction-unlimited all-optical imaging and writing with a photochromic GFP. *Nature* **478**, 204–208 (2011).
16. Testa, I. et al. Nanoscopy of living brain slices with low light levels. *Neuron* **75**, 992–1000 (2012).
17. Bohm, U., Hell, S. W. & Schmidt, R. 4Pi-RESOLFT nanoscopy. *Nat. Commun.* **7**, 10504 (2016).
18. Grotjohann, T. et al. rsEGFP2 enables fast RESOLFT nanoscopy of living cells. *eLife* **1**, e00248 (2012).
19. Pennacchietti, F. et al. Fast reversibly photoswitching red fluorescent proteins for live-cell RESOLFT nanoscopy. *Nat. Methods* **15**, 601–604 (2018).
20. Chmyrov, A. et al. Nanoscopy with more than 100,000 'doughnuts'. *Nat. Methods* **10**, 737–740 (2013).
21. Masullo, L. A. et al. Enhanced photon collection enables four dimensional fluorescence nanoscopy of living systems. *Nat. Commun.* **9**, 3281 (2018).
22. Rego, E. H. et al. Nonlinear structured-illumination microscopy with a photoswitchable protein reveals cellular structures at 50-nm resolution. *Proc. Natl Acad. Sci. USA* **109**, E135–E143 (2012).
23. Li, D. et al. Extended-resolution structured illumination imaging of endocytic and cytoskeletal dynamics. *Science* **349**, aab3500 (2015).
24. Xue, Y. & So, P. T. C. Three-dimensional super-resolution high-throughput imaging by structured illumination STED microscopy. *Opt. Express* **26**, 20920–20928 (2018).
25. Mahecic, D., Testa, I., Griffie, J. & Manley, S. Strategies for increasing the throughput of super-resolution microscopies. *Curr. Opin. Chem. Biol.* **51**, 84–91 (2019).
26. Stiel, A. C. et al. 1.8 Angstrom bright-state structure of the reversibly switchable fluorescent protein dronpa guides the generation of fast switching variants. *Biochem. J.* **402**, 35–42 (2007).
27. Bodén, A., Casas Moreno, X., Cooper, B. K., York, A. G. & Testa, I. Predicting resolution and image quality in RESOLFT and other point scanning microscopes [Invited]. *Biomed. Opt. Express* **11**, 2313–2327 (2020).
28. van Niel, G., D'Angelo, G. & Raposo, G. Shedding light on the cell biology of extracellular vesicles. *Nat. Rev. Mol. Cell Biol.* **19**, 213–228 (2018).
29. Chan, D. C. Mitochondria: dynamic organelles in disease, aging, and development. *Cell* **125**, 1241–1252 (2006).
30. Ding, W. X. et al. Electron microscopic analysis of a spherical mitochondrial structure. *J. Biol. Chem.* **287**, 42373–42378 (2012).
31. Miyazono, Y. et al. Uncoupled mitochondria quickly shorten along their long axis to form indented spheroids, instead of rings, in a fission-independent manner. *Sci. Rep.* **8**, 350 (2018).
32. Meyer, D., Bonhoeffer, T. & Scheuss, V. Balance and stability of synaptic structures during synaptic plasticity. *Neuron* **82**, 430–443 (2014).
33. Masch, J. M. et al. Robust nanoscopy of a synaptic protein in living mice by using organic-fluorophore labeling. *Proc. Natl Acad. Sci. USA* **115**, E8047–E8056 (2018).
34. Hruska, M., Henderson, N., Le Marchand, S. J., Jafri, H. & Dalva, M. B. Synaptic nanomodules underlie the organization and plasticity of spine synapses. *Nat. Neurosci.* **21**, 671–682 (2018).
35. Tao-Cheng, J. H., Thein, S., Yang, Y., Reese, T. S. & Gallant, P. E. Homer is concentrated at the postsynaptic density and does not redistribute after acute synaptic stimulation. *Neuroscience* **266**, 80–90 (2014).
36. Spahn, C., Grimm, J. B., Lavis, L. D., Lampe, M. & Heilemann, M. Whole-cell, 3D, and multicolor STED imaging with exchangeable fluorophores. *Nano Lett.* **19**, 500–505 (2019).
37. Booth, M. J. Adaptive optical microscopy: the ongoing quest for a perfect image. *Light Sci. Appl.* **3**, e165 (2014).

Methods

3D pRESOLFT setup. Images from 3D pRESOLFT are acquired using a custom-built microscope based on conventional optical and electro-optical components. A schematic of the optical setup is found in Supplementary Fig. 3, and it can be divided into three main paths: (1) creation of multifocal patterns for ON-switching (405-nm laser) and readout (488-nm laser); (2) creation of the OFF-switching pattern (491-nm laser); and (3) detection of images of the emitted fluorescence by a scientific complementary metal oxide semiconductor (sCMOS) camera. Both microlens patterns are generated by a fiber-coupled laser source (Cobolt 06-MLD 488 and 405 nm filtered with Chroma ET405/10X and ET488/10X, respectively). The fiber output passes through a collimating lens and the collimated beam then hits the microlens array (Thorlabs, MLA150-7AR-M) with a distance 150 μm between lenslets. The image plane behind the microlenses is demagnified by a factor of 2 using a 4f telescope. The beams are then coupled into the main optical path using a 50/50 non-polarizing beam splitter (Thorlabs, CCM1-BS013/MB) for the 488-nm path and a dichroic mirror (Semrock Di03-R442-t1-25×36) for the 405-nm path. The main optical path contains an optimized tube lens and one of the following objective lenses: ×100/1.4 numerical aperture (NA) Leica STED-Orange oil or ×100/1.35 NA Nikon silicon, giving around ×104 demagnification. The final periodicity of the multifocal pattern in the sample is 720 nm.

The OFF-switching path initially consists of three separate paths originating from two different, but identical, laser sources (Cobolt Calypso 491-nm diode-pumped solid-state). Using a 50/50 polarizing beam splitter (Thorlabs CCM1-PBS251/M), one of the beams is divided in two to give the total of three beams. Two of these, beams 1 and 2, have horizontal polarization while the third, beam 3, has vertical polarization. Beams 1 and 2 are directed onto a diffraction grating (phase-diffraction gratings of 437-nm-high SiO_2 lines with a 25-μm period (Laser Laboratorium Göttingen)) with horizontal grating lines. These beams will create the partial pattern P_1 and P_2 shown in Fig. 1c. The mirrors preceding the diffraction grid are placed so that these beams hit the grid at an angle of 1.125° but in opposite directions (Supplementary Fig. 3). This small tilt at the plane of the diffraction grids is what provides asymmetry in the back focal plane. Since these two beams originate from different laser sources, they will be temporally incoherent and thus will not interfere with one another. Beam 3 is directed onto a diffraction grating with vertical grating lines. This beam is aligned symmetrically with the optical axis and creates the partial pattern P_3. After passing through the two gratings, the beams are combined with a second polarizing beam splitter. The combined beams pass through a telescope between which a physical mask is placed to block everything except the +1 and −1 diffraction orders of the gratings. Since the −1 order of beam 1 and +1 order of beam 2 will both fall on the optical axis at the plane of the mask and must not be impeded, while the 0 order of beam three should be blocked, a very small intentional misalignment of beam 3 is introduced to allow blocking of the 0 order without blocking the −1 and +1 order of beams 1 and 2, respectively. Although this will introduce a minor tilt in the partial pattern P_3, it will have no notable influence on the final pattern and performance of the system. For calculations of final pattern periodicities, see Supplementary Note 7.3. The detection is designed as a conventional widefield microscope. Because the main excitation path is reflected off a long-pass dichroic mirror (Semrock Di03-R488-t1-25×36) before entering the objective, the fluorescent light emitted will pass through the dichroic mirror and be imaged onto a sCMOS camera (Hamamatsu ORCA-Fusion) using a standard 200-mm tube lens. The detection path also contains an additional bandpass filter (Chroma ET535/70 m), to minimize any ambient light, and two notch filters (Chroma ZET405NF and ZET488NF), to eliminate any reflections.

All imaging parameters related to the presented data are illustrated in Supplementary Table 5.

Image reconstruction and processing. To reconstruct a final image (2D or 3D) from the raw 3D pRESOLFT data, the emission from each confined volume in each frame must be quantified. The array of emission volumes in the sample in each scan cycle is imaged onto the camera sensor, resulting in an array of diffraction-limited PSFs. From previous knowledge of illumination patterns, the center of each PSF is known and the camera frame is segmented into subregions, each containing a single detected PSF. Each subregion is then processed individually and the intensity of the central PSF is quantified by least-squares fitting of a centered Gaussian function on top of a constant background in the same way as was done in our previous work[21]. Important to note is that the scanning is done purely by moving the sample. The light patterns are stationary and thus the emission pattern seen on the camera is also stationary. The final image corresponds to the coefficients associated with the central diffraction-limited Gaussian from the fits. The reconstruction algorithm is implemented in Python with GPU-accelerated CUDA (compute unified device architecture) processing and reconstructs full volumetric data within seconds.

Deconvolution and effective PSF. Given accurate modeling of the photoswitching properties of reversibly switchable fluorescent proteins (as reported in detail in Supplementary Note 3.4), the image formation model can be concisely described as a convolution between sample fluorophore density and the derived effective PSF with added noise. This accurate description of the image formation process allows for estimation of the underlying sample density using the Richardson–Lucy algorithm. The deconvolved images are labeled with an asterisk (*), like 3D pRESOLFT*, and the number of iterations is reported. The precise description of the effective PSF proves essential to achieving accurate deconvolution results (Supplementary Note 5 and Supplementary Fig. 9). Furthermore, by accurate calculation of the effective PSF for given imaging parameters, deconvolution allows for substantial increases in image contrast at the highest spatial frequencies. Deconvolution is performed using a custom script implemented in Python that allows for easy adaptation of the effective PSF to the imaging parameters used. The effective PSF used for deconvolution and for fitting of line profiles can be described as the sum of a wider diffraction-limited Gaussian function and a narrow, super-resolved Gaussian. According to the photophysical and image formation model outlined, the amplitude of the larger confocal Gaussian is generally considered to be up to 30% of the global PSF and 350–400 nm wide axially (further consideration on line fitting is reported in Supplementary Note 4). In particular, for deconvolution a central Gaussian of $85×85×120$ nm³ was used in combination with a larger Gaussian of $165×165×400$ nm³, accounting for 18% of total amplitude.

Sample preparation. *Epithelial cell culture and RSFP plasmids.* U2OS (ATCC HTB-96™) cells were cultured in DMEM (Thermo Fisher Scientific, no. 41966029) supplemented with 10% (vol/vol) fetal bovine serum (Thermo Fisher Scientific, no. 10270106), 1% penicillin/streptomycin (Sigma-Aldrich, no. P4333) and maintained at 37 °C and 5% CO_2 in a humidified incubator. For transfection, $2×10^5$ cells per well were seeded on coverslips on a six-well plate. After 1 d, cells were transfected using FuGENE (Promega, no. E2311) according to the manufacturer's instructions. At 24–36 h after transfection, cells were washed in PBS solution, placed with phenol-red-free Leibovitz's L-15 Medium (Thermo Fisher Scientific, no. 21083027) in a chamber and imaged. The following plasmids were used for exogenous expression: rsEGFP2-Omp25, LifeAct-rsEGFP2 and endogenously tagged vimentin-rsEGFP2 cell lines[38]. To label exosomes, the construct CD63-rsEGFP2 was generated by exchanging EGFP from plasmid CD63_OHu03119C_pcDNA3.1(+)-C-eGFP (GenScript Biotech). Briefly, the rsEGFP2 coding sequence was amplified from a template[21] using the primer pair 5′- atgatcgcggccgcGTGAGCAAGGGCGAGGAGCTG and 5′-gatcattctagaTTACTTGTACAGCTCGTCCATGC. Both backbone and insert were digested using NotI-HF and XbaI (NEB) separately, followed by T4 ligation (NEB) and transformation of NEB Stable cells (NEB). Plasmids were prepared from the transformants and verified via Sanger sequencing.

Metabolic treatments. Antimycin A (Sigma-Aldrich, no. A8674-25MG) was added to cells during the imaging experiment, at 40 μM final concentration, then cells were imaged for up to 1 h. CCCP (Sigma-Aldrich, no. C2759-100MG) was then added to cells during the experiment, at 10 μM final concentration, and cells were imaged 1–3 and 30–36 min afterwards.

Hippocampal neuron cultures. Primary hippocampal cultures were prepared from embryonic E18 Sprague–Dawley rat embryos. Hippocampi were dissected and mechanically dissociated in MEM. Next, $20×10^3$ cells per well were seeded in 12-well plates on a poly-D-ornithine (Sigma-Aldrich, no. P8638)-coated no. 1.5, 18-mm glass coverslips (Marienfeld) and allowed to adhere in MEM with 10% horse serum (Thermo Fisher Scientific, no. 26050088), 2 mM L-Glut (Thermo Fisher Scientific, no. 25030-024) and 1 mM sodium pyruvate (Thermo Fisher Scientific, no. 11360-070). After 3 h the medium was exchanged for Neurobasal (Thermo Fisher Scientific, no. 21103-049) supplemented with 2% B-27 (Thermo Fisher Scientific, no. 17504-044), 2 mM L-glutamine and 1% penicillin/streptomycin. Experiments were performed on cultures >22 days in vitro. At 12–24 h before experiments, cells were infected with a modified Semliki forest virus expressing the postsynaptic density protein homer or actin cytoskeleton, together with the photoswitchable proteins Drompa(M159T), Homer1c-Dronpa(M159T) and LifeAct-Dronpa(M159T)), by direct addition of virus to the culture medium. To induce long-term potentiation, neurons were treated with 25 mM (final concentration) of the potassium channel blocker tetraethylammonium chloride (TEA-Cl; Sigma-Aldrich, no. T2265-25G) for 10 min (ref. 39) then washed in artificial cerebrospinal fluid and imaged after 30 min. All experiments were performed in accordance with the animal welfare guidelines of Karolinska Institutet and were approved by Stockholm North Ethical Evaluation Board for Animal Research.

RSFP functionalized beads. Silica beads with a diameter of 500 nm and with Ni-ntrilotriacetic acid (Ni-NTA) functional groups on the surface were obtained from Micromod Partikeltechnologie. Silica beads with a diameter of 2.5 μm were acquitred from Bang Laboratories. Brain-sphingomyelin, cholesterol and 1,2-dioleoyl-sn-glycero-3-[(N-(5-amino-1-carboxypentyl)iminodiacetic acid) succinyl] (nickel salt) were purchased from Avanti Polar Lipids. rsEGFP2 protein was expressed in *Escherichia coli* strain BL21-CP-RIL and purified by Ni-NTA affinity chromatography (His SpinTrap, GE Healthcare) according to the manufacturer's instructions. The purified protein was concentrated in a buffer

of 100 mM Tris-HCl, 150 mM NaCl pH 7.5. For rsEFGP2 functionalization of 500-nm silica beads, the affinity between the His-tag sequence of the protein and the Ni-NTA groups was utilized, the protocol being based simply on mixing of the binding partners. The amount of the protein required was calculated assuming unitary binding efficiency and one protein molecule per 75 nm^2 of bead surface. Briefly, an aliquot of 50 μl of a 50 mg ml^{-1} dispersion of 500-nm silica beads was mixed in a vial with 46 μl of buffer (500 mM NaCl, 20 mM NaH$_2$PO$_4$ pH 7.85) and 4 μl of a 41 μM solution of purified rsEGFP2 protein. The mixture was incubated at room temperature for 30 min, then 4 μl of the mixture was dropped on a coverslip and a glass slide pressed over. The sample was sealed with a two-component silicone glue (Twinsil, Picodent).

Image analysis. *Mitochondrial morphology classification.* To quantify the observed changes in the mitochondrial network induced by treatment with antimycin A or CCCP, mitochondria were classified according to their morphology into tubular, MDVs, fragments or spheroids (Fig. 5b). The difference between the three first types relates to the relative dimension of the three axes by which mitochondrial shape can be described: d_x, d_y and d_z. A shape is considered tubular when two axes are very similar and smaller than the third: $d_x \cong d_y < d_z$. If all three axes are similar in size and <350 nm: $d_x \cong d_y \cong d_z < 350$ nm, the mitochondrion is considered to be an MDV. When the mitochondrion is >350 nm in all three dimensions and has a single spherical shape, it is defined as a fragment. Lastly, what distinguishes a spheroid from a fragment—otherwise similar in terms of axis ratio—is the presence of an inner luminal structure that allows one to define two distinct volumes (those used to define the ratio as in Fig. 5c). The volumes are calculated using the three axes and assuming an ellipsoidal shape. Given 3D pRESOLFT* volumetric recordings at different time points of the treatment, the numbers of mitochondria falling into each of these four categories were counted by visual inspection (*n* = 3).

Quantification of homer nanovolumes. To analyze the morphology of each cluster of homers in its 3D distribution, we first localized their centroids using the ImageJ plugin 3D objects counter[40], which identifies them on the base of an intensity threshold. For each centroid a cube of $1.05 \times 1.05 \times 1.05$ μm^3 is considered and the enclosed intensity distribution of the homer cluster is fitted to a 3D Gaussian function. The volume reported in the histogram is therefore that of the ellipsoid enclosed by the fitted 3D Gaussian. For the time-lapse recording shown in Fig. 6c–e, each cluster in the first frame was associated with the same cluster in the second frame using a proximity threshold <500 nm, accounting for possible shifting of images during the 40-min incubation time following LTP induction. The same applies to the comparison between confocal and 3D pRESOLFT, since the acquisition of the two volumes is sequential in time and therefore a small shift can occur between the two volumetric images.

Reporting Summary. Further information on research design is available in the Nature Research Reporting Summary linked to this article.

Data availability
The data that support the findings of this study are available from the corresponding author upon reasonable request.

Code availability
The software used to acquire the super-resolved data (hardware control, image reconstruction and deconvolution pipeline) were developed by our laboratory and available upon request.

References
38. Ratz, M., Testa, I., Hell, S. W. & Jakobs, S. CRISPR/Cas9-mediated endogenous protein tagging for RESOLFT super-resolution microscopy of living human cells. *Sci. Rep.* **5**, 9592 (2015).
39. Hosokawa, T., Rusakov, D. A., Bliss, T. V. & Fine, A. Repeated confocal imaging of individual dendritic spines in the living hippocampal slice: evidence for changes in length and orientation associated with chemically induced LTP. *J. Neurosci.* **15**, 5560–5573 (1995).
40. Bolte, S. & Cordelieres, F. P. A guided tour into subcellular colocalization analysis in light microscopy. *J. Microsc.* **224**, 213–232 (2006).

Author contributions
I.T. designed and supervised the project. A.B. engineered and built the microscope with associated software. A.B. performed the experiments and data analysis. F.P. carried out RSFP switching experiments and data analysis. G.C. and M.D. performed the bioimaging treatments and imaging. M.R. cloned the constructs and provided biological guidance. I.T. and A.B. wrote the manuscript with assistance from all the authors.

Competing interests
I.T. and A.B. have filed a provisional patent on the 3D pRESOLFT technology (no. N.1930406-2, Sweden, December 2019).

Additional information
Supplementary information is available for this paper at https://doi.org/10.1038/s41587-020-00779-2.

Correspondence and requests for materials should be addressed to I.T.

Peer review information *Nature Biotechnology* thanks Reto Fiolka, Valentin Nagerl and the other, anonymous, reviewer(s) for their contribution to the peer review of this work.

Reprints and permissions information is available at www.nature.com/reprints.

Corresponding author(s):   Ilaria Testa

Last updated by author(s):   Nov 13, 2020

Reporting Summary

Nature Research wishes to improve the reproducibility of the work that we publish. This form provides structure for consistency and transparency in reporting. For further information on Nature Research policies, see our Editorial Policies and the Editorial Policy Checklist.

Statistics

For all statistical analyses, confirm that the following items are present in the figure legend, table legend, main text, or Methods section.

n/a	Confirmed	
☐	☒	The exact sample size (*n*) for each experimental group/condition, given as a discrete number and unit of measurement
☐	☒	A statement on whether measurements were taken from distinct samples or whether the same sample was measured repeatedly
☒	☐	The statistical test(s) used AND whether they are one- or two-sided *Only common tests should be described solely by name; describe more complex techniques in the Methods section.*
☒	☐	A description of all covariates tested
☒	☐	A description of any assumptions or corrections, such as tests of normality and adjustment for multiple comparisons
☒	☐	A full description of the statistical parameters including central tendency (e.g. means) or other basic estimates (e.g. regression coefficient) AND variation (e.g. standard deviation) or associated estimates of uncertainty (e.g. confidence intervals)
☒	☐	For null hypothesis testing, the test statistic (e.g. *F*, *t*, *r*) with confidence intervals, effect sizes, degrees of freedom and *P* value noted *Give P values as exact values whenever suitable.*
☒	☐	For Bayesian analysis, information on the choice of priors and Markov chain Monte Carlo settings
☒	☐	For hierarchical and complex designs, identification of the appropriate level for tests and full reporting of outcomes
☒	☐	Estimates of effect sizes (e.g. Cohen's *d*, Pearson's *r*), indicating how they were calculated

Our web collection on statistics for biologists contains articles on many of the points above.

Software and code

Policy information about availability of computer code

Data collection	For the imaging, the control of the hardware are part of our open-source microscope control project developed in Python available at https://github.com/TestaLab/3D-pRESOLFT_code We used Python v.3.5
Data analysis	For reconstruction of the images we used a custom built reconstruction software together with a Richardson-Lucy deconvolution script available at https://github.com/TestaLab/3D-pRESOLFT_code We used Python v.3.5 For image analysis of Homer nanovolumes we used: ImageJ v.1.53c Plugin: 3D Object counter v.2.0

For manuscripts utilizing custom algorithms or software that are central to the research but not yet described in published literature, software must be made available to editors and reviewers. We strongly encourage code deposition in a community repository (e.g. GitHub). See the Nature Research guidelines for submitting code & software for further information.

Data

All manuscripts must include a data availability statement. This statement should provide the following information, where applicable:

- Accession codes, unique identifiers, or web links for publicly available datasets
- A list of figures that have associated raw data
- A description of any restrictions on data availability

No restriction on data availability. The data that support the findings of this study are available from the corresponding author upon reasonable request.

Field-specific reporting

Please select the one below that is the best fit for your research. If you are not sure, read the appropriate sections before making your selection.

☒ Life sciences   ☐ Behavioural & social sciences   ☐ Ecological, evolutionary & environmental sciences

For a reference copy of the document with all sections, see nature.com/documents/nr-reporting-summary-flat.pdf

Life sciences study design

All studies must disclose on these points even when the disclosure is negative.

Sample size	No sample size dependent statistical testing was performed
Data exclusions	No data were excluded from the analysis.
Replication	The quality of images presented was reproducible in different days of recording and for extended times after system alignment. System alignment was stable time and only some days required minor realignment at the start of a days recording.
Randomization	No allocation into experimental group were performed
Blinding	No allocation into experimental group were performed

Reporting for specific materials, systems and methods

We require information from authors about some types of materials, experimental systems and methods used in many studies. Here, indicate whether each material, system or method listed is relevant to your study. If you are not sure if a list item applies to your research, read the appropriate section before selecting a response.

Materials & experimental systems

n/a	Involved in the study
☒	☐ Antibodies
☐	☒ Eukaryotic cell lines
☒	☐ Palaeontology and archaeology
☐	☒ Animals and other organisms
☒	☐ Human research participants
☒	☐ Clinical data
☒	☐ Dual use research of concern

Methods

n/a	Involved in the study
☒	☐ ChIP-seq
☒	☐ Flow cytometry
☒	☐ MRI-based neuroimaging

Eukaryotic cell lines

Cell line source(s)	U2OS cell line from ATCC
Authentication	None of the cell lines used have been authenticated
Mycoplasma contamination	All cell lines tested negative for mycoplasma contamination
Commonly misidentified lines (See ICLAC register)	No commonly misidentified cell lines were used in this study

Animals and other organisms

Laboratory animals

primary neuronal cell dissociated from rat fetuses hippocampi, Sparague Dawley Rat, Age: embryonic day 18

Wild animals

Field-collected samples

Ethics oversight

All experiments in neuronal culture are in accordance with animal welfare guidelines set forth by Karolinska Institutet and were approved by Stockholm North Ethical Evaluation Board for Animal Research.

Note that full information on the approval of the study protocol must also be provided in the manuscript.